Hybrid Mixture Theory Based Modeling of Transport Mechanisms and Expansion-Thermomechanics of Starch During Extrusion

Srivikorn Ditudompo and Pawan S. Takhar
Food Science and Human Nutrition, University of Illinois at Urbana-Champaign, Urbana, IL, 61801

DOI 10.1002/aic.14936
Published online July 22, 2015 in Wiley Online Library (wileyonlinelibrary.com)

Water, vapor, and heat transport mechanisms and thermomechanical changes occurring inside the expanding extrudate were described using hybrid mixture theory-based unsaturated transport equations. Transport equations were transformed from the Eulerian coordinates to the Lagrangian coordinates. Good agreements between the predicted and experimental values of surface temperature, moisture content, and expansion ratio of the extrudates were obtained. The model was also used to calculate temperature, moisture content, pore-pressure, and viscoelastic-stress distribution in the extrudate. Matrix collapse and glassy crust formation under the surface was calculated as a function of extrusion conditions. Expansion behavior of the extrudate was described using the difference between stress due to pore pressure and viscoelastic stress. The modeling results can serve as a guide for predictably modifying the extrusion parameters for obtaining specific textural attributes of expanded starch for various food, feed, and biomedical applications. © 2015 American Institute of Chemical Engineers *AIChE J*, 61: 4517–4532, 2015
Keywords: hybrid mixture theory, multiphase porous media, unsaturated transport, poroviscoelasticity, extrusion

Introduction

Starch is a low cost, abundantly available renewable biopolymer. Expansion of starch exiting the die of an extruder has been widely used for production of various biodegradable materials useful in agricultural, medical, and biotechnological applications. Expansion is an important phenomenon that affects the structural, mechanical, and textural characteristics of the extruded products. Expansion involves various phenomena such as phase transition, glass transition, nucleation, bubble growth and collapse, and evaporative cooling.[1] When the starch wetted with plasticizer (water or blowing agent) is processed in an extruder, it is subjected to various degrees of shearing, heating, and mixing along a single or a pair of screws as it approaches toward the end of screws. Starch granules break down to various degrees, forming a melt. This melt, when further passed through a restriction (die nozzle), is subjected to more shear and is finally released to the atmosphere. Just before exiting the die, water or blowing agent exists in a superheated state due to high pressure in the final stages of extrusion. Due to low pressure outside the extruder, some liquid evaporates to vapor phase. The extrudate first undergoes swelling due to bubble growth and then collapses due to elastic recovery.[2–6] As this process happens, the starch melt and plasticizer undergo phase changes along with release in pressure and drop in temperature (due to evaporative cooling) resulting in a final porous plastic like structure. Expansion is a very critical process that determines the final extrudate characteristics.

Several studies have concentrated on relating the final (stable) expansion of product with extrusion conditions such as screw speed, mechanical energy input, extrusion temperatures, and die design[3,4,6–11]; with material properties such as moisture content[2,10–13]; with starch composition and source[10]; with system parameters such as residence time distribution[3,6,14,15]; with viscosity of the melt in die[16–19]; with specific mechanical energy[20,21]; and with molecular weight reduction.[21,22] Reviews on the dependence of expansion on various processing parameters during extrusion were performed by Lai and Kokini,[18] Kokini et al.,[23] Colonna et al.,[24] Harper and Tribelhorn,[25] and Mitchell and Areas.[26] In spite of a large amount of experimental work, expansion has not been adequately explained and modeled due to complexity of the underlying heat- and fluid-transfer processes. It is important to model this process to be able to predictably control the properties of extruded product. The process involves multiscale characteristics, which cannot be addressed adequately using single-scale equations with various assumptions as attempted in the literature (see, e.g., Ref. 27). Several attempts have been made to model expansion of polymers during extrusion.[1,27–30] Park[2] and Kokini et al.[5] described the phenomena of extrudate expansion by accounting for bubble growth as the main cause. The effect of extrudate swell was neglected. Shafi et al.[29] explained that the main causes of free expansion of polymer foaming were nucleation and bubble growth. Fan et al.[28] accounted for heat and moisture losses to the surroundings from an expanding bubble cell and concluded that during

Pawan S. Takhar has previously published as Pawan P. Singh.

Correspondence concerning this article should be addressed to P. S. Takhar at ptakhar@illinois.edu

expansion, the temperature of extrudate decreases rapidly while the glass transition temperature increases. They concluded that melt viscosity was the dominant factor resisting cell growth and shrinkage and that the surface tension effect was negligible. The melt elasticity was neglected and vapor pressure was considered to be the only factor affecting expansion. Mao et al.[31] noted that a realistic model for foam expansion should involve macroscale flow information, microscale (same as our mesoscale) bubble growth dynamics governed by pressure and concentration gradients and bubble diffusion equations. After making comparison of model predictions to experiments, they conclude that future works should consider replacement of specific pressure forms and Henry's law with more general equations. These studies provide an excellent insight into the physical mechanisms involved in expansion. However, most studies used single-scale approaches and focused on a given type of mechanism because it was difficult to study all the factors using experimental methods or single-scale modeling approaches. Lee[27] compiled various expansion models used in extrusion of polymeric foams, which are also based upon single-scale approaches. Wang et al.[30] developed a model for describing the nonisothermal expansion in starch-based foams during extrusion. The nucleation of bubbles, bubble growth, and diffusion of water vapors from the starch matrix into the bubbles occurred at a microscopic level and extrudate expansion occurred at a macroscopic level. In contrast, the hybrid mixture theory (HMT) is used in this manuscript, which involves a generalized framework of multiscale equations based upon the laws of continuum thermodynamics. This helps to avoid paradoxes, which are prone to arise in unsaturated porous media problems (such as foam expansion) formulated using conventional approaches.[32]

Many methods are available for incorporating multiscale phenomena.[33,34] In methods such as matched asymptotic expansion[34] and volume averaging in the sense of Whitaker,[35] constitutive equations are formulated at the microscale (of the order microns). Although, this captures the microscale physics, the material coefficients in equations also need to be measured at this scale. These material coefficients are difficult to determine because of the difficulties involved in devising experiments at microscale. HMT involves using the mathematical filtering theorems[33] to average the microscale field equations twice to obtain equations at the meso and macroscales. First, microscale equations are averaged over the solid-vicinal fluid domain to obtain the mesoscale equations. At mesoscale, equations are further averaged over the solid-fluid mixture and bulk phases to obtain equations at the macroscale. At macroscale, constitutive equations are formulated by exploiting the entropy inequality in the sense of Coleman and Noll.[36] During upscaling (averaging), some microscale information is lost. However, the effect of microscale transport mechanisms and thermomechanical processes on macroscale behavior is incorporated. One significant advantage of upscaling is that material coefficients in equations show up at the macroscale, which are easier to measure via macroscale experiments or obtain from other experimental studies using conventional methods. Upscaled equations are solved in macro and mesoscale representative elementary volumes (REV), which saves the computational time significantly in comparison to time needed for solving the microscale equations. HMT was initially used to explain the thermomechanical behavior of swelling and shrinking porous media like clays.[37–39] Singh et al.[40,41] applied HMT, to swelling biopolymeric systems with viscoelastic behavior. Recently, Takhar[42] used HMT to obtain transport and thermomechanical relations for biopolymers subjected to unsaturated transport processes.

In this study, the extrudate is considered as a poroviscoelastic medium composed of three phases: solid, liquid water, and gas (mixture of water vapors and dry air). At microscale, the solid and fluid phases of the material are considered as viscoelastic and viscous, respectively. At macroscale, the interaction between the viscoelastic solid and the viscous fluids in pores results in a poroviscoelastic matrix.[42] The developed model can be used to understand the unsaturated transport mechanisms involved during extrusion and to identify the effect of process parameters on the properties of extruded starch. It will be useful to reduce design time and raw material wastage involved in running the trial and error experiments in the production of starch-based products. This modeling approach integrated with the relevant experimental work, developed in this study, will be useful to improve the design and to optimization of the extrusion process of starches and other biopolymers.

In order to describe the expansion phenomenon adequately, this study uses the two-scale HMT-based equations of Takhar[42] coupled with the poroviscoelasticity equations for predicting the transport processes and mechanical changes in the extrudates during expansion. The modeling results for the surface temperature, moisture content, and expansion ratio are compared with the experimental results in order to assess the validity of the extruded expansion model. In addition, the temperature, moisture and pressure profiles, stress profiles, and glass transition behavior are plotted and used to elucidate the expansion mechanisms.

Mathematical Model

System description

Figure 1 is a three-scale (micro, meso, and macro) representation of starch composed of solid, liquid, and vapor phases. At the microscale (of the order of microns), the solid (predominantly amylose and amylopectin chains) and vicinal liquid (water or blowing agent adsorbed on the solid surface) are distinct from each other (in walls of starch cells). Nucleation of bubbles in expanding starch occurs in micropores of nucleating agents. It is affected by the roughness and porosity of the nucleating agents and thermodynamic equilibrium among solid, liquid, and gas phases.[43] Liquid phase on a nucleation site follows its surface contours, thus exerting greater influence on the phase equilibria than the macroscale boundaries. At mesoscale (of the order of millimeters), solid and vicinal liquids are homogenized together and cannot be distinguished from each other. In addition, domains of bulk water (or blowing agent) and vapor phase are present. Properties of the vicinal liquid such as chemical potential, specific heat, and viscosity may be different from the bulk phases because of its adsorption over the solid surface. At mesoscale, the phenomena affecting bubble growth and starch expansion are intermolecular forces between the biopolymers and fluid phases,[44] capillary forces in mesopores,[43] and the exchange of thermodynamic properties between various phases.[40] At mesoscale, different microscale nucleation sites compete and coalesce with each other. At the macroscale, the starch cells are homogenized with domains of bulk liquid and vapor phases to form a homogeneous mixture at each microsized spatial point. The capillary forces in the macropores and macroscale

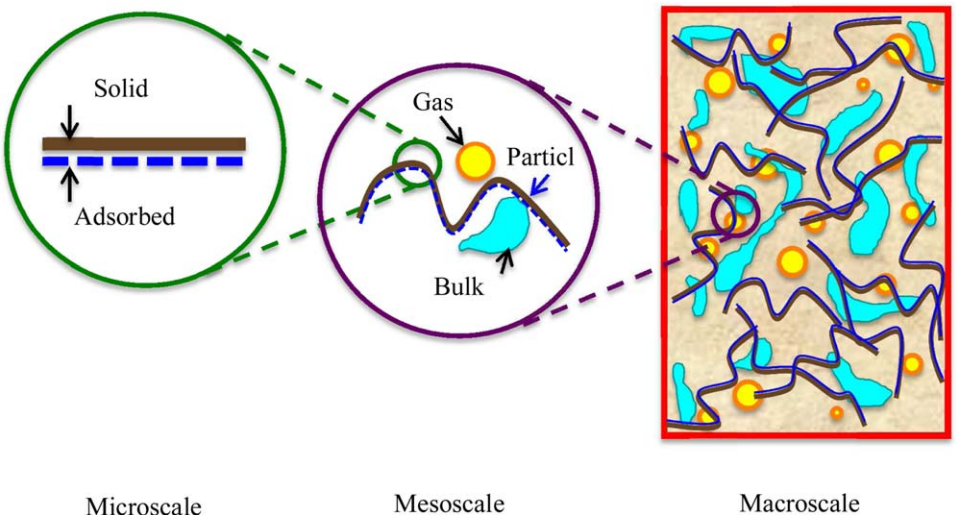

Figure 1. Three-scale structure of the extrudate.

Particle denotes solid polymers together with adsorbed fluid. [Color figure can be viewed in the online issue, which is available at wileyonlinelibrary.com.]

heterogeneities affect the liquid and vapor transport, and starch expansion.

After the cornstarch melt exits the die, the solid matrix expands to form a porous structure because the expanding vapors and moving liquids interact with the solid wall. These interactions are partially driven by the physical pressure difference between the inside and the exterior of the matrix.

In analyzing the mass- and energy-transfer changes in the deforming extruded starch during expansion, the following assumptions were made—the extrudate was considered as a poroviscoelastic material, which consisted of viscoelastic solid matrix and viscous water and gas in pores; the extrudate was assumed to be a homogeneous, linear viscoelastic, and isotropic porous material inside the macroscale REV; both solid and liquid water phases were assumed to be the incompressible at microscale (macroscale matrix expansion was still allowed) while the gas phase (the mixture of water vapor and dry air) was assumed to be a compressible fluid; the effect of gravity was neglected; the extrudate was cylindrically symmetric when it exited the die and remained so for the entire expansion process; the various phases were at local thermal equilibrium inside the macroscale REV; the extrudate expansion was due to the generation of internal pressure in the pores; and the effect of thermal radiation on the convective flow was not considered.

Generalized multiphase transport equations

The generalized Darcy's law can be coupled with the mass balance equations to derive the generalized transport equations for various phases.[40,41,45] The two-scale mass balance equation for the α-phase is[42]

$$\frac{D^{s}(\varepsilon^{\alpha}\rho^{\alpha})}{Dt}+\nabla_{E}\cdot(\varepsilon^{\alpha}\rho^{\alpha}\mathbf{v}_{E}^{\alpha,s})-\varepsilon^{\alpha}\rho^{\alpha}\frac{\dot{\varepsilon}^{s}}{\varepsilon^{s}}=\sum_{\substack{\beta=w,g\\ \beta\neq\alpha}}{}^{\beta}\hat{e}^{\alpha},\quad \text{where } \alpha=w,g \tag{1}$$

where D^{s}/Dt and dot over a variable ($\dot{\varepsilon}^{s}$) represent material time derivative with respect to the solid phase, ε^{α} and ε^{s} are the volume fractions of the α and solid phases, respectively, ρ^{α} is the density of the α-phase, ∇_{E} is the spatial gradient in Eulerian coordinates, $\mathbf{v}_{E}^{\alpha,s}=\mathbf{v}_{E}^{\alpha}-\mathbf{v}_{E}^{s}$ is the Eulerian velocity of the α-phase relative to the solid phase, and ${}^{\beta}\hat{e}^{\alpha}$ is the net rate of mass gained by transferring a quantity from the β-phase to the α-phase. At mesoscale, the mass exchange occurs only between the water and gas (in term of vapors) phases due to evaporation or condensation. Therefore, ${}^{w}\hat{e}^{g}$ is nonzero for $\alpha = w, g$.

For the water-phase transport, it is assumed that the water phase is incompressible at the microscale, which makes $\dot{\rho}^{w}=0$ in Eq. 1, and it simplifies to

$$\dot{\varepsilon}^{w}\rho^{w}+\nabla_{E}\cdot(\varepsilon^{w}\rho^{w}\mathbf{v}_{E}^{w,s})-\varepsilon^{w}\rho^{w}\frac{\dot{\varepsilon}^{s}}{\varepsilon^{s}}=-{}^{w}\hat{e}^{g} \tag{2}$$

For problems involving the phase change, the mass gained by liquid phase (condensation term—${}^{w}\hat{e}^{g}$) is equal to the mass lost by the gas phase (${}^{g}\hat{e}^{w}$).

The gas phase is compressible at the microscale ($\dot{\rho}^{g}\neq 0$). Thus, the gas-phase mass balance is

$$\varepsilon^{g}\dot{\rho}^{g}+\dot{\varepsilon}^{g}\rho^{g}+\nabla_{E}\cdot(\varepsilon^{g}\rho^{g}\mathbf{v}_{E}^{g,s})-\varepsilon^{g}\rho^{g}\frac{\dot{\varepsilon}^{s}}{\varepsilon^{s}}={}^{w}\hat{e}^{g} \tag{3}$$

Similarly, as the gas is a mixture of air and vapors, the mass balance equation for the vapor phase is

$$\varepsilon^{v}\dot{\rho}^{v}+\dot{\varepsilon}^{v}\rho^{v}+\nabla_{E}\cdot(\varepsilon^{v}\rho^{v}\mathbf{v}_{E}^{v,s})-\varepsilon^{v}\rho^{v}\frac{\dot{\varepsilon}^{s}}{\varepsilon^{s}}={}^{w}\hat{e}^{v} \tag{4}$$

where ${}^{w}\hat{e}^{v}={}^{w}\hat{e}^{g}$.

The solid phase is assumed to be incompressible ($\dot{\rho}^{s}=0$) at microscale. The mass balance equation for solid phase is[40]

$$\dot{\varepsilon}^{s}+\varepsilon^{s}\nabla_{E}\cdot\mathbf{v}_{E}^{s}=0 \tag{5}$$

The volume fraction constraint for the material can be written as

$$\varepsilon^{s}+\varepsilon^{w}+\varepsilon^{g}=1 \tag{6}$$

The sum of volume fraction of water and gas is equal to the porosity (ϕ), $\varepsilon^{w}+\varepsilon^{g}=\phi$. Therefore, the ε^{s} and $\dot{\varepsilon}^{s}$ terms in Eqs. 1–5 can be replaced by porosity using the relations $\varepsilon^{s}=1-\phi$ and $\dot{\varepsilon}^{s}=-\dot{\phi}$. In addition, the volume fraction of the gas is equal to the volume fraction of the vapor and air ($\varepsilon^{g}=\varepsilon^{v}=\varepsilon^{a}$). Therefore, the ε^{g} can replace ε^{v} in Eq. 4.

Generalized Darcy's law relations

The generalized Darcy's law relation for the water phase for the isotropic biopolymers with a short-memory can be written as[42]

$$\mathbf{v}_{\mathrm{E}}^{\mathrm{w,s}} = -\left(\varepsilon^{\mathrm{w}}\frac{K^{\mathrm{w}}}{\mu^{\mathrm{w}}}\nabla_{\mathrm{E}}p^{\mathrm{w}} + \varepsilon^{\mathrm{w}}D^{\mathrm{w}}\nabla_{\mathrm{E}}\varepsilon^{\mathrm{w}} + \varepsilon^{\mathrm{w}}\frac{K^{\mathrm{w}}}{\mu^{\mathrm{w}}}N^{\mathrm{w}}\nabla_{\mathrm{E}}\dot{\varepsilon}^{\mathrm{w}}\right) \quad (7)$$

During unsaturated transport in biopolymers, the velocity of fluid flow is directly proportional to the pressure and concentration gradients, which is represented by the first and second terms on RHS. The last term on RHS represents the mixture viscosity effect of polymers. The permeability of water (K^{w}) is related to the diffusivity of water (D^{w}) via the relation[42]: $K^{\mathrm{w}} = D^{\mathrm{w}}\mu^{\mathrm{w}}/E$.

The velocity of gas phase was represented using

$$\mathbf{v}_{\mathrm{E}}^{\mathrm{g,s}} = -\varepsilon^{\mathrm{g}}\frac{K^{g}}{\mu^{g}}\nabla_{\mathrm{E}}p^{\mathrm{g}} \quad (8)$$

The velocity of vapor phase was represented using

$$\mathbf{v}_{\mathrm{E}}^{\mathrm{v,s}} = \mathbf{v}_{\mathrm{E}}^{\mathrm{g,s}} + \mathbf{v}_{\mathrm{E}}^{\mathrm{v,g}} \quad (9)$$

with

$$\mathbf{v}_{\mathrm{E}}^{\mathrm{v,g}} = -\frac{D^{\mathrm{v}}}{\omega^{\mathrm{v}}}\nabla_{\mathrm{E}}\omega^{\mathrm{v}} \quad (10)$$

where $\mathbf{v}_{\mathrm{E}}^{\mathrm{v,g}}$ represents the binary diffusion for the mixture of vapor and air[46] and $\omega^{\mathrm{v}} = \rho^{\mathrm{v}}/(\rho^{\mathrm{a}} + \rho^{\mathrm{v}})$.

Energy balance

The energy transfer within the porous material was assumed to be driven by the convection due to moving phases, heat conduction, and phase change.[45,47] It was represented using[48]

$$\sum_{\alpha=\mathrm{s,w,g}}\varepsilon^{\alpha}\rho^{\alpha}C_{\mathrm{p}}^{\alpha}\frac{D^{\alpha}T}{Dt} = \nabla_{\mathrm{E}}\cdot\left(\sum_{\alpha=\mathrm{s,w,g}}(\varepsilon^{\alpha}k^{\alpha})\nabla_{\mathrm{E}}T\right) - \lambda^{\mathrm{w}}\hat{e}^{\mathrm{g}} \quad (11)$$

The following equation can be used to modify the material time derivative with respect to the α-phase to with respect to the solid phase

$$\frac{D^{\alpha}T}{Dt} = \frac{D^{\mathrm{s}}T}{Dt} + \mathbf{v}_{\mathrm{E}}^{\alpha,\mathrm{s}}\cdot\nabla_{\mathrm{E}}T \quad (12)$$

where the material time derivative of temperature following the velocity of a particle in solid phase is related to the spatial time derivative by

$$\frac{D^{\mathrm{s}}T}{Dt} = \frac{\partial T}{\partial t} + \mathbf{v}_{\mathrm{E}}^{\mathrm{s}}\cdot\nabla_{\mathrm{E}}T \quad (13)$$

Therefore, the energy balance Eq. 11 can be written as

$$\sum_{\alpha=\mathrm{s,w,g}}\varepsilon^{\alpha}\rho^{\alpha}C_{\mathrm{p}}^{\alpha}\left(\frac{\partial T}{\partial t} + \mathbf{v}_{\mathrm{E}}^{\alpha}\cdot\nabla_{\mathrm{E}}T\right) = \nabla_{\mathrm{E}}\cdot\left(\sum_{\alpha=\mathrm{s,w,g}}(\varepsilon^{\alpha}k^{\alpha})\nabla_{\mathrm{E}}T\right) - \lambda^{\mathrm{w}}\hat{e}^{\mathrm{g}} \quad (14)$$

where the Eulerian velocity of the α-phase is calculated using the relation: $\mathbf{v}_{\mathrm{E}}^{\alpha} + \mathbf{v}_{\mathrm{E}}^{\alpha,\mathrm{s}} + \mathbf{v}_{\mathrm{E}}^{\mathrm{s}}$.

The first term on LHS of Eq. 14 is the energy storage term and the second term on LHS represents energy convection due to movement of various phases across the REV boundary. On RHS, the first term represents energy conduction and the second term represents source/sink of energy due to evaporation/condensation.

Poroviscoelastic equations

Deformation of the extrudate was calculated from the displacement field. The linear momentum balance for an isotropic mixture of solid and fluids can be written as[49]

$$\sum_{\alpha=\mathrm{s,w,g}}\rho^{\alpha}\frac{\partial^2\mathbf{u}}{\partial t^2} - \nabla_{\mathrm{L}}\cdot\boldsymbol{\sigma} = \mathbf{F}_{\mathrm{b}} \quad (15)$$

where $\boldsymbol{\sigma}$ is the stress tensor, $\mathbf{F}_{\mathrm{b}}$ is the body force, and $\mathbf{u} = \mathbf{u}(r,\theta,z)$ is the displacement field in cylindrical coordinates of a material point attached to the solid matrix. The displacement field is considered as the dependent variable in Eq. 15. The displacement field was calculated as a function of internal stress in the porous matrix. For the cylindrical arrangement, the displacement in the θ direction was neglected because the material points were assumed not to rotate in the expanding extrudate.

The mechanical stress in the material was described as a linear viscoelastic stress. The total stress tensor comprised stress due to pore pressure ($\boldsymbol{\sigma}_{\mathrm{p}}$) and viscoelastic stress ($\boldsymbol{\sigma}_{\mathrm{viscoelas}}$)

$$\boldsymbol{\sigma} = \boldsymbol{\sigma}_{\mathrm{p}} + \boldsymbol{\sigma}_{\mathrm{viscoelas}} \quad (16)$$

where $\sigma_p = -p_{\mathrm{p}}\mathbf{I} = -\sum_{\alpha=w,g}s^{\alpha}p^{\alpha}\mathbf{I}$ and

$$\boldsymbol{\sigma}_{\mathrm{viscoelas}}(t) = \int_0^{\mathrm{t}}G(t-\tau)\frac{\partial\boldsymbol{\varepsilon}(\tau)}{\partial\tau}d\tau \quad (17)$$

where $G(t) = G_{\infty} + \sum_{\mathrm{m}=1}^{\mathrm{n}}G_{\mathrm{m}}e^{-\mathrm{t}/\tau_{\mathrm{m}}}$

After the extrudate exits the die, the pore pressure (p_{p}), which is the average pressure exerted by the fluids contained within the pores on the solid walls, is suddenly developed in the matrix and can be used to calculate the stress due to pore pressure ($\boldsymbol{\sigma}_{\mathrm{p}}$).[50] In addition, pore pressure can be used as the variable governing expansion and shrinkage in the extrudate matrix. It is represented using $p_{\mathrm{p}} = s^{\mathrm{w}}p^{\mathrm{w}} + s^{\mathrm{g}}p^{\mathrm{g}}$.[51]

Generalized Maxwell model was used to model the viscoelastic response of the extrudate. It consists of an elastic element in parallel with the Maxwell elements.[52] For viscoelastic stress, G(t) is the stress relaxation function, τ is the relaxation time, G_{∞} is the modulus of the equilibrium spring element, n is the number of Maxwell units, G_{m} is the relaxation modulus of the mth spring element, and τ_{m} is the relaxation time of the mth dashpot.

The components of the nonlinear strain tensor can be expressed in terms of the displacement field ($\mathbf{u}$) as[53]

$$\boldsymbol{\varepsilon}_{\mathrm{ij}} = \frac{1}{2}\left(\nabla_{\mathrm{i}}\mathbf{u}_{\mathrm{j}} + \nabla_{\mathrm{j}}\mathbf{u}_{\mathrm{i}} + \nabla_{\mathrm{i}}\mathbf{u}_{\mathrm{m}}\nabla_{\mathrm{j}}\mathbf{u}_{\mathrm{m}}\right) \quad (18)$$

Transforming Eulerian to Lagrangian coordinates

After extrudate leaves the die, expansion occurs due to the pressure difference between the inside and the exterior of the extruded matrix. Therefore, expansion of starch involves solving the moving boundary problem. The system of equations was transformed from Eulerian to Lagrangian (or material) coordinates.

It was assumed that the solid phase of the material is incompressible at microscale. The differential volume (dv) in deformed material is related to the initial undeformed differential volume (dV) by[54]

$$dv = j dV \tag{19}$$

where j is the determinant of the Jacobian matrix. For an unsaturated system, j can be written as[42]

$$j = \frac{\varepsilon_0^s}{\varepsilon^s} = \frac{1-\phi_i}{1-\phi} \tag{20}$$

The extrudate was assumed to be of cylindrical shape so the Eq. 19 becomes

$$r\, dr\, d\theta\, dz = jR\, dR\, d\Theta\, dZ \tag{21}$$

When a cylinder in Lagrangian coordinates is transformed to a cylinder in Eulerian coordinates or vice versa, the shape of extrudate was assumed to remain geometrically similar ($r = \zeta R$ and $z = \zeta Z$). Additionally, the material points were assumed not to rotate in the angular direction during volume change ($d\theta = d\Theta$). Therefore, using $dr/dR = dz/dZ = r/R = \zeta$, the Eq. 21 becomes

$$j = \zeta^3 \tag{22}$$

In axisymmetric cylindrical coordinates, the Eulerian gradient operator can be written as

$$\nabla_E \equiv \frac{\partial}{\partial r}\hat{e}_r + \frac{\partial}{\partial z}\hat{e}_z \tag{23}$$

Using the chain rule, the relation between gradient operator in Eulerian and Lagrangian coordinates can be expressed as

$$\nabla_E = \frac{\partial R}{\partial r}\frac{\partial}{\partial R}\hat{e}_R + \frac{\partial Z}{\partial z}\frac{\partial}{\partial Z}\hat{e}_Z = \frac{\partial R}{\partial r}\left(\frac{\partial}{\partial R}\hat{e}_R + \frac{\partial}{\partial Z}\hat{e}_Z\right) = \frac{1}{\zeta}\nabla_L \tag{24}$$

where $dR/dr = 1/\zeta$ and $\nabla_L \equiv \frac{\partial}{\partial R}\hat{e}_R + \frac{\partial}{\partial Z}\hat{e}_Z$. The displacement coefficient ζ is a function of volume fraction of solid (or porosity) at a given spatial coordinate. By substituting $\zeta = j^{1/3}$ in Eq. 24, we obtain

$$\nabla_E = j^{-1/3}\nabla_L = \left(\frac{1-\phi}{1-\phi_i}\right)^{1/3}\nabla_L \tag{25}$$

Using Eq. 25, the mass balance equations 2–5, momentum balance equations 7–10, and heat balance equation 14 can be transformed to the Lagrangian coordinates as

Water phase

$$\dot{\varepsilon}^w \rho^w + \left(\frac{1-\phi}{1-\phi_i}\right)^{1/3}\nabla_L \cdot (\varepsilon^w \rho^w \mathbf{v}_L^{w,s}) + \varepsilon^w \rho^w \frac{\dot{\phi}}{1-\phi} = -{}^w\hat{e}^v \tag{26}$$

where $\mathbf{v}_L^{w,s} = -\left(\frac{1-\phi}{1-\phi_i}\right)^{1/3}\left(\varepsilon^w \frac{K^w}{\mu^w}\nabla_L p^w + \varepsilon^w D^w \nabla_L \varepsilon^w + \varepsilon^w \frac{K^w}{\mu^w} N^w \nabla_L \dot{\varepsilon}^w\right)$.

Gas phase

$$\varepsilon^g \dot{\rho}^g + \dot{\varepsilon}^g \rho^g + \left(\frac{1-\phi}{1-\phi_i}\right)^{1/3}\nabla_L \cdot (\varepsilon^g \rho^g \mathbf{v}_L^{g,s}) + \varepsilon^g \rho^g \frac{\dot{\phi}}{1-\phi} = {}^w\hat{e}^v \tag{27}$$

where $\mathbf{v}_L^{g,s} = -\left(\frac{1-\phi}{1-\phi_i}\right)^{1/3}\varepsilon^g \frac{K^g}{\mu^g}\nabla_L p^g$.

Vapor phase

$$\varepsilon^g \dot{\rho}^v + \dot{\varepsilon}^g \rho^v + \left(\frac{1-\phi}{1-\phi_i}\right)^{1/3}\nabla_L \cdot (\varepsilon^g \rho^v \mathbf{v}_L^{v,s}) + \varepsilon^g \rho^v \frac{\dot{\phi}}{1-\phi} = {}^w\hat{e}^v \tag{28}$$

where $\mathbf{v}_L^{v,s} = \mathbf{v}_L^{g,s} + \mathbf{v}_L^{v,g}$ and $\mathbf{v}_L^{v,g} = -\left(\frac{1-\phi}{1-\phi_i}\right)^{1/2}\frac{D}{\omega^v}\nabla_L \omega^v$.

Solid phase

$$\dot{\phi} - (1-\phi)\left(\frac{1-\phi}{1-\phi_i}\right)^{1/3}\nabla_L \cdot \mathbf{v}_L^s = 0 \tag{29}$$

Energy balance

$$\sum_{\alpha=s,w,g}\varepsilon^\alpha \rho^\alpha C_p^\alpha \left(\frac{\partial T}{\partial t} + \mathbf{v}_L^\alpha \cdot \left(\frac{1-\phi}{1-\phi_i}\right)^{1/3}\nabla_L T\right) \left(\frac{1-\phi}{1-\phi_i}\right)^{1/3}\nabla_L \cdot \left(\frac{1-\phi}{1-\phi_i}\right)^{1/3}\left(\sum_{\alpha=s,w,g}(\varepsilon^\alpha k^\alpha)\nabla_L T\right) - \lambda^w \hat{e}^v \tag{30}$$

where $\mathbf{v}_L^\alpha = \mathbf{v}_L^{\alpha,s} + \mathbf{v}_L^s$.

Equations 26–30 coupled with the poroviscoelasticity Eq. 15 can be used to solve the unsaturated transport problems for the deforming biopolymeric materials.

Input parameters and material properties

All physical, thermal, and mechanical properties of materials required to solve the transport equations are given in Tables 1–3.

Volume Fraction of Water. The relation of the moisture content and volume fraction of water in the extrudate can be calculated as

$$\varepsilon^w = \frac{X_w \rho_s (1-\varepsilon^g)}{X_w \rho_s + \rho_w} \tag{31}$$

Evaporation/Condensation Term. The source/sink term due to phase change can be calculated using[61]

$${}^w\hat{e}^g = {}^w\hat{e}^v = \xi\left(p_{eq}^v - p^v\right) \tag{32}$$

where ξ represents the evaporation rate constant, $p_{eq}^v = a_w p_{sat}$ is the equilibrium vapor pressure, a_w is the water activity of the matrix (Table 3) and p_{sat} is the saturated vapor pressure at a given temperature (Table 1). The p^v is calculated using the thermodynamic relation: $p^v = \rho^v R^v T$, where the ρ^v is the dependent variable obtained by solving the Eq. 28.

Capillary Pressure. The generalized Darcy's law relations (Eq. 7) involve flow of water due to both concentration gradient ($\nabla\varepsilon^w$) and pressure gradient (∇p^w). The capillary pressure relation can be used to calculate p^w from p^g and p^c

$$p^g - p^w = p^c \tag{33}$$

where the following relationship between capillary pressure (p^c) and water-phase saturation (s^w) is used[72,73]

$$p^c = 101325\left[12.12\, s^w \exp(-5.939\, s^w) + 0.046(1-s^w)(s^w)^{-3.7}\right]\left[1 - 2.79\times10^{-3}(T-273)\right] \tag{34}$$

Heat- and Mass-Transfer Coefficients. After the extrudate exits the die, convective heat and mass transfer occurs between the extrudate surface and the surrounding air. The water and vapor fluxes can be determined using the partial pressure of vapors across the extrudate surface[74] as shown in Table 4. In convection heat-transfer studies, a ratio of heat convection relative to heat conduction across the fluid layer can be written in terms of the Nusselt number as

Table 1. Physical, Thermal, and Mechanical Properties of Materials Used in the Model

Property		Source
Coefficient of diffusivity ($m^2\ s^{-1}$)		
Water	$2.9\times10^{-8}\exp\left(-13.9/(R_uT)\right)$	Vagenas and Karathanos[55]
Vapor	$-2.775\times10^{-6}+4.479\times10^{-8}T+1.656\times10^{-10}T^2$	By fitting to data from Bolz and Tuve[56]
Density ($kg\ m^{-3}$)		
Air	Ideal gas	
Water	$838.466+1.401T-3.011\times10^{-3}T^2+3.718\times10^{-7}T^3$	Poling et al.[57]
Molecular weight (kg/mol^{-1})		
Air	28.97×10^{-3}	Denny[58]
Water	18.02×10^{-3}	Denny[58]
Vapor	18.02×10^{-3}	Denny[58]
Specific heat ($J\ kg^{-1}\ K^{-1}$)		
Air	$1047.637-0.373T+9.453\times10^{-4}T^2-6.024\times10^{-7}T^3+1.286\times10^{-10}T^4$	Poling et al.[57]
Water	$12010.147-80.407T+0.310T^2-5.382\times10^{-4}T^3+3.625\times10^{-7}T^4$	Zábranský et al.[59]
Vapor	$13604.734-90.430T+0.277T^2-4.213\times10^{4}T^3+3.184\times10^{-7}T^4-9.561\times10^{-11}T^5$	Poling et al.[57]
Thermal conductivity ($W\ m^{-1}\ K^{-1}$)		
Air	$-2.276\times10^{-3}+1.155\times10^{-4}T-7.903\times10^{-8}T^2+4.117\times10^{-11}T^3-7.439\times10^{-15}T^4$	Vargnaftik[60]
Water	$0.869+8.949\times10^{-3}T-1.584\times10^{-5}T^2+7.975\times10^{-9}T^3$	Vargnaftik[60]
Vapor	$1.317\times10^{-4}+5.150\times10^{-5}T+3.896\times10^{-8}T^2-1.368\times10^{-11}T^3$	Vargnaftik[60]
Viscosity (Pa s)		
Air	$-8.383\times10^{-7}+8.357\times10^{-8}T-7.694\times10^{-11}T^2+4.644\times10^{-14}T^3-1.066\times10^{-14}T^4$	Poling et al.[57]
Water	$1.380-2.122\times10^{-2}T+1.360\times10^{-4}T^2-4.645\times10^{-7}T^3+8.904\times10^{-10}T^4-9.079\times10^{-13}T^4+3.846\times10^{-16}T^6$	Poling et al.[57]
Vapor	$1.420\times10^{-6}+3.835\times10^{-8}T-3.852\times10^{-12}T^2+2.102\times10^{-15}T^3$	Poling et al.[57]
Evaporation rate constant ($s\ m^{-2}$) $\xi=0.5$		Fang and Ward[61]
Latent heat of vaporization ($J\ kg^{-1}$) $\lambda=2.792\times10^6-160T-3.43T^2$		Stanish et al.[62]
Mixture viscosity (Pa s) $N^w=1.12\times10^3[9826.208-14215.012X_w+(35.883X_w-18.326)T]$		Adapted from Ditudompo et al.[63]
Saturated vapor pressure (Pa) $p_{sat}=\exp\left[\begin{array}{c}-6096.939T^{-1}+21.241-2.711\times10^{-2}T\\+1.67\times10^{-5}T^2+2.434\log(T)\end{array}\right]$		Perry and Green[64]
Universal gas constant ($J\ mol^{-1}\ K^{-1}$) $R_u=8.314462$		

$$Nu=\frac{h_TL}{k^g} \tag{35}$$

where h_T is the heat-transfer coefficient ($W\ m^{-2}\ K^{-1}$), L is the length of material, and k^g is the thermal conductivity of gas phase ($W\ m^{-1}\ K^{-1}$). This number can be used to calculate the heat-transfer coefficient when Nu, L, and k^g are known. Yang[75] expressed the experimental results of axial thermal convection along a cylinder using the following relation

$$Nu=\left[0.6\left(\frac{L}{D}\right)^{0.5}+0.387\left(\frac{Ra}{\left[1+(0.492/Pr)^{9/16}\right]^{16/9}}\right)^{1/6}\right]^2 \tag{36}$$

where D is the diameter of material, Ra is the Rayleigh number $\left(Ra=\frac{g\beta(T-T_{atm})L^3Pr}{(\mu^g/\rho^g)^2}\right)$, β is, β is thermal expansion coefficient ($\beta=1/T_f$), and Pr is Prandtl number $\left(Pr=C_p^g\mu^g/K^g\right)$. All

Table 2. Physical and Thermal Properties of Gas (Mixture of Water Vapor and Dry Air)

Property	Equation	Source
Specific heat ($J\ kg^{-1}\ K^{-1}$)	$C_p^g=\omega^aC_p^a+\omega^vC_p^v$ where $\omega^a=1-\omega^v$ and $\omega^v=\frac{\rho^v}{\rho^a+\rho^v}$	Chapman-Enskog theory[46]
Gas permeability (m^2)	$K^g=1.01\times10^{-3}\exp(-10.86s^w)$ where $s^w=\frac{\varepsilon^w}{\varepsilon^w+\varepsilon^g}$	Ni et al.[65] and Feng et al.[66]
Thermal conductivity ($W\ m^{-1}\ K^{-1}$)	$k^g=\frac{X^ak^a}{X^v\Phi^{av}+X^a}+\frac{X^vk^v}{X^a\Phi^{va}+X^v}$ where $X^a=1-X^v$, $X^v=\frac{p^v}{p^g}$, $\Phi^{va}=\frac{[1+(\mu^v/\mu^a)^{0.5}(M^a/M^v)^{0.25}]}{8^{0.5}(M^v/M^a)^{0.5}}$ and $\Phi^{av}=\frac{[1+(\mu^v/\mu^a)^{0.5}(M^a/M^v)^{0.25}]}{8^{0.5}(M^v/M^a)^{0.5}}$	Chapman-Enskog theory[46]
Viscosity (Pa s)	$\mu^g=\frac{X^a\mu^a}{X^v\Phi^{av}+X^a}+\frac{X^v\mu^v}{X^a\Phi^{va}+X^v}$	Chapman-Enskog theory[46]

Table 3. Geometry and Physical, Thermal, and Mechanical Properties of the Extrudates

Property	Unit	Equation or value	Source
Initial diameter	m	3×10^{-3}	Measured
Initial length	m	4.5×10^{-3}	Measured
True density	kg m^{-3}	1423.7	Measured
Specific heat	J kg^{-1} K^{-1}	$2570.1X_w - 1694.4$	By fitting to data from Hwang et al.[67]
Water activity		$\exp[-5.9\times10^{-3}/X_w^{(629/250)}]$	Modified Halsey model[68] by fitting to data from Ditudompo et al.[63]
Thermal conductivity	W m^{-1} K^{-1}	$0.21+4.1\times10^{-4}T$	Maroulis et al.[69]
Coefficient of elasticity	MPa	1.7	Fan et al.[70]
Poisson ratio		0.3	Agbisit et al.[71]
Viscoelastic parameters	Pa	$G_1=2.52\times10^4$	By fitting to data from Ditudompo et al.[63]
(Generalized Maxwell model)	Pa	$G_2=1.52\times10^4$	
	s	$\tau_1=10.9$	
	s	$\tau_2=123.7$	

gas phase properties are evaluated at the film temperature of $T_f = (T + T_{atm})/2$. The range of h_T calculated using (36) are given in Table 4.

The convective mass-transfer coefficient (h_m) for forced convection of the fluid flow across a single cylinder are given by[64]

$$h_m = 0.692 Re^{-0.486} v^g Sc^{-0.644} \tag{37}$$

where Reynolds and Schmidt numbers for the gas flow parallel to the cylinder axis are expressed as $Re = v^g \rho^g L/\mu^g$ and $Sc = \mu^g/\rho^g D^v$. The properties of gas phase are evaluated at the film temperature.

In addition, the mass and heat transfer are analogous phenomenon under certain conditions. The coefficients of mass and heat transfer are related by Lewis analogy and can be expressed as[76]

$$\frac{h_T}{h_m} = \rho^g C_p^g Le^{2/3} \tag{38}$$

where Le is the Lewis number, $Le = (Sc/Pr)$. This analogy is valid for liquids and gases within the range of $0.6 < Sc < 2500$ and $0.6 < Pr < 100$. For this study, both forced and natural convection relations, and Eqs. 37 and 38 were used depending upon the range of air velocities and dimensionless numbers.

Glass Transition Temperature. Zhong and Sun[77] used the differential scanning calorimeter (DSC) to determine the thermal behavior of gelatinized cornstarch in a moisture content range of 13.5–31.6% (db). Their study showed that the gelatinized cornstarch undergoes glass transition at 19.1–98.3°C. Similar results were observed by Shogren,[78] and Ditudompo et al.[63] Prediction of glass transition temperature of gelatinized cornstarch (T_{gl}) was obtained using the Gordon–Taylor equation[79]

$$T_{gl} = \frac{X_{bw} T_{gl}^w + c_{gl}(1 - X_{bw}) T_{gl}^s}{X_{bw} + c_{gl}(1 - X_{bw})} \tag{39}$$

where X_{bw} is the mass fraction of pure water, c_{gl} is a constant, and T_{gl}^w and T_{gl}^s are the glass transition temperatures of pure water and pure starch, respectively. For pure water, T_{gl}^w is taken as 138.2 K. Zhong and Sun[77] reported the values of c_{gl} and T_{gl}^s are 0.176 and 551.0 K, respectively. Additionally, the X_{bw} is defined as the bound water or nonfreezing water that is tightly bound to the gelatinized cornstarch molecules and

Table 4. Initial and Boundary Conditions and Experimental Parameters of the Extrudates Extruded at Feed Moisture Content of 26.1% (db), Barrel Temperature of 413.2 K, and Screw Speed of 300 rpm

Property	Equation	Quantity
Water transport	26	IC: IC : $\varepsilon^w = \varepsilon_i^w$ BC: at $r = R$; water flux $Q_w = -h_m(\rho_{eq}^v - \rho_{amb}^v)$ (kg m^{-2} s^{-1}) with $h_m = 0.097-0.125$ (m s^{-1}) where $\rho_{eq}^v = \frac{p_{eq}^v}{R^v T}$, $R^v = \frac{R_u}{M^v}$, $\rho_{amb}^v = \frac{p_{amb}^v}{R^v T} = \frac{R_H p_{sat,T_{amb}}}{R^v T}$ and $p_{sat,T_{amb}}$ is the saturated vapor pressure at T_{amb}.
Gas transport	27	IC: $p_i^g = p_i^v + p_i^a$ (Pa) where $p_i^v = a_{w,T_i} p_{sat,T_i}$, a_{w,T_i} is the water activity at T_i, P_{sat,T_i} is the saturated vapor pressure at T_i, $p_i^a = \rho_i^a R^a T_i$, ρ_i^a is the air density at T_i, and $R^a = R_u/M^a$. BC: at $r = R$; $p^g = p_{amb}$[pa] (Pa)
Vapor diffusion	28	IC: $\rho_i^v = \frac{p_i^v}{R^v T_i}$ (kg m^{-3}) BC: at $r = R$; vapor flux $Q_v = -h_m(\rho^v - \rho_{amb}^v)$ (kg m^{-2} s^{-1})
Solid mass balance	29	IC: $\phi = \phi_i$
Energy transfer	30	IC: $T = T_i$ (K) BC: at $r = R$; heat flux $Q_T = h_T(T - T_{amb})$ (W m^{-2}) with $h_T = 3.59-159.0$ (W m^{-2} K^{-1})
Poroviscoelastic	15	IC: $\boldsymbol{\sigma}_i = -(s^w p^w + s^g p^g)\mathbf{I}$ (Pa) $U_{r,i} = \mathbf{0}$ and $U_{z,i} = 0$(m) BC: at $r = R$ and $z = Z$; $p = p_{amb}$ (Pa)
Ambient parameters:		
Ambient pressure		$p_{amb} = 101325$(Pa)
Ambient temperature		$T_{amb} = 298.15$(K)
Relative humidity		$R_H = 0.45$
Extrudate properties at initial state:		
Moisture content		$Xwi = 0.213$ (kg_{solid}^{-1})
Porosity		$\phi_i = \varepsilon_i^w + \varepsilon_i^g = 0.284$
Temperature		$T_i = 419.3$ (K)
Volume fraction of gas		$\varepsilon_i^g = 0.048$
Volume fraction of water		$\varepsilon_i^w = 0.236$

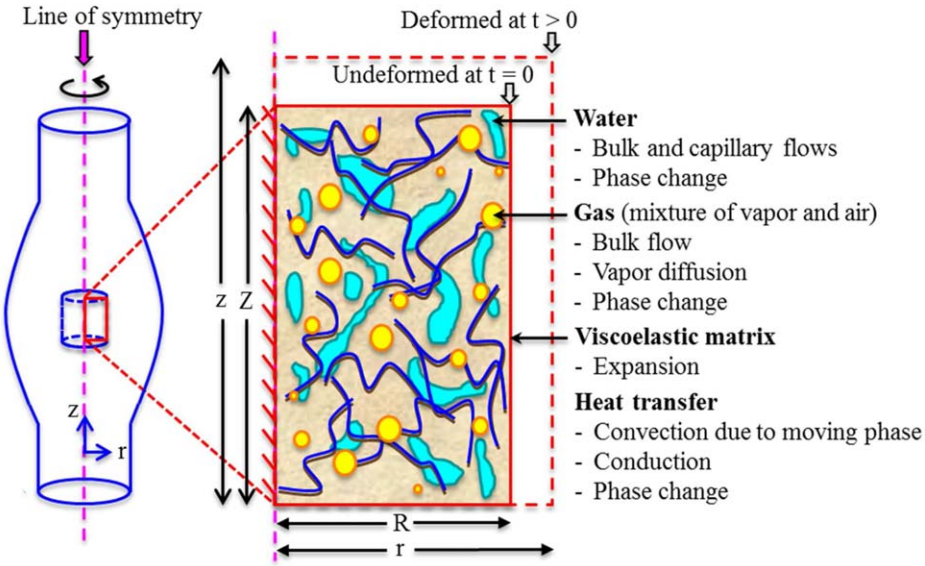

Figure 2. Schematic diagram of the extrudate showing the fluid and heat transfer during expansion.

[Color figure can be viewed in the online issue, which is available at wileyonlinelibrary.com.]

cannot be crystallized to ice. It can be determined using the DSC and expressed as gram of water per gram of dry starch.[77]

Initial and boundary conditions

The initial moisture content of the extrudates at different extrusion conditions were measured after exiting the die to be 0.143–0.245 $kg_{solid}kg_{solid}^{-1}$. The volume fraction of water phase was calculated using the Eq. 31 and the initial volume fraction of gas phase was estimated by using the difference between the moisture content of the feed mixtures and initial moisture content of the extrudates at the die exit. Various initial and boundary conditions and experimental parameters needed to obtain the solution of the transport model for extrudate during expansion are summarized in Table 4.

Materials and Methods

Experimental procedures

Extrudate samples were prepared from native cornstarch (Tate & Lyle Ingredients Americas LLC, Decatur, IL) with initial moisture content of 8.7% (db). The cornstarch was blended with distilled water, adjusted to moisture content of 19 and 27% (db) and then stored in a refrigerator for 24 h to equilibrate the moisture. The average moisture content of the equilibrated samples were 18.3 ± 0.5 and $26.1 \pm 0.5\%$ (db), respectively. Next, the cornstarch samples were extruded with a twin-screw extruder (C.W. Brabender Instrument, South Hackensack, NJ) with a screw diameter of 1.8 cm and a screw length of 80 cm. The die nozzle had a single circular hole with a diameter of 3 mm. The mixtures were fed manually at feed rates consistent with the preset screw speed of 200, 300, and 400 rpm. The temperature of the three heating zones of the extruder barrel and die were maintained at 323.2, 393.2, 393.2 K; and 323.2, 413.2 and 413.2 K, respectively. Temperatures and pressures for each extrusion condition were set and recorded automatically by the extruder heating and cooling system (PL 2000 Controller, C.W. Brabender Instrument). In this study, the temperatures of melted blends at the end of the extruder barrel were expressed as extrusion temperatures. After the extrudates exited the die, they were collected at 1, 5, 10, 20, and 40 s and immediately immersed in the liquid nitrogen for 1 min.

Moisture content of extrudates was determined by gravimetric method.[63] The samples were dried in an air oven at 105°C for 24 h and cooled to room temperature in a desiccator. Moisture content (% dry basis) is presented as an average of six measurements.

An infrared ThermaCAM SC640 camera (FLIR systems, Inc., Boston, MA, USA) was used to record the two-dimensional (2-D) images of the extrudates after exiting the die, which were recorded under steady-state conditions for every 0.05 s for 2 min. ThermaCAM Researcher Pro 2.10 Analysis Software (FLIR systems) was used to analyze the infrared images for determining the temperature distribution on the surface of extrudates. For each image, the surface temperature along the length of extrudate was defined as the maximum temperature in each section along the length. Each reported value is an average of 10 measurements. The expansion of the sample was evaluated on the basis of diameter change. The expansion ratio was calculated by dividing the cross-sectional diameter of the extrudate by the cross-sectional diameter of the die nozzle. For analyzing the infrared images, an image analysis software (ImageJ, Ver 1.48; National Institutes of Health, Bethesda, MD) was used for measuring the diameter along the length of each extrudate. An average expansion ratio of 10 measurements is reported. Further details about experimental procedure are given in Ditudompo.[80]

Numerical solution and model validation

The extrudate was assumed to be of cylindrical shape. Therefore, a 2-D-axisymmetric finite element geometry was used for the simulations (Figure 2). A commercial finite elements software package (COMSOL Multiphysics Ver 4.4; Comsol, Burlington, MA) was used for solving the mass-, momentum-, and heat-transfer equations coupled with the poroviscoelasticity equations in order to investigate the extruded cornstarch during expansion. A mapped mesh was generated at time zero with predefined distribution type and 100 elements with an element ratio (ratio of center to surface element length) of 5. The solution was achieved using the

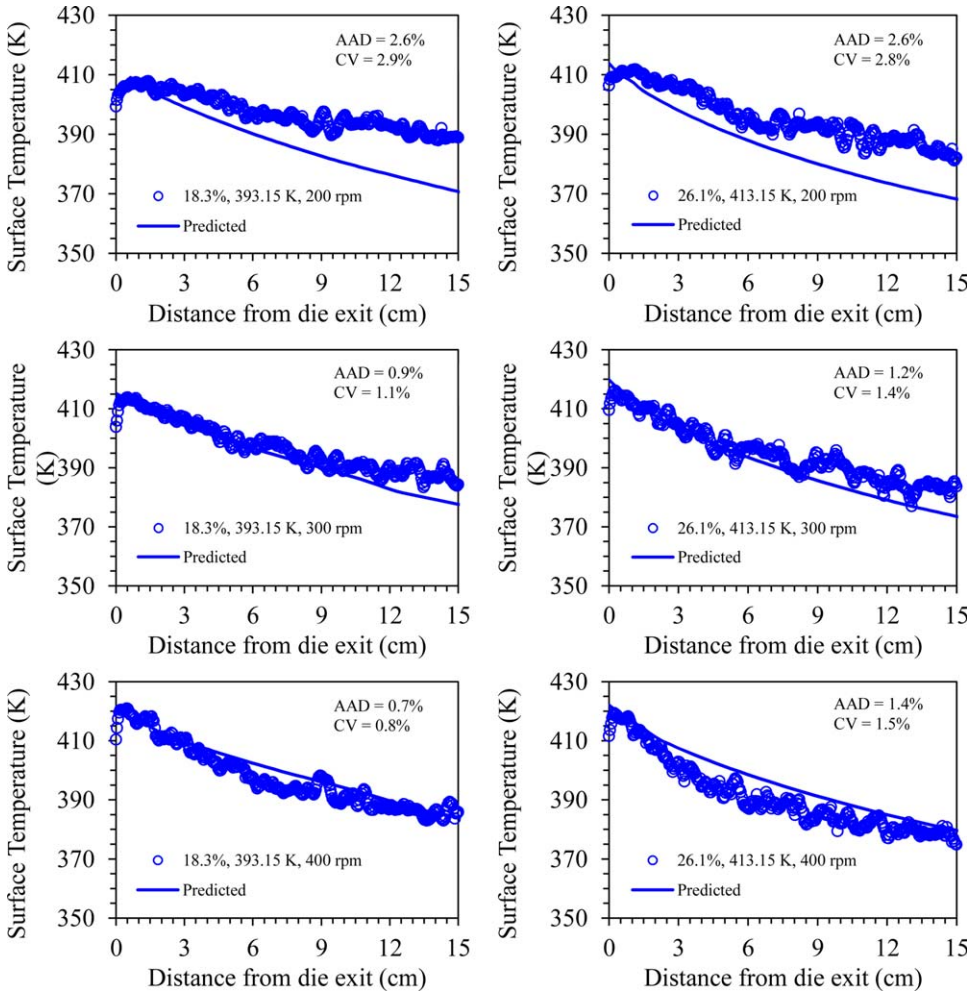

Figure 3. Comparison of experimental and predicted surface temperature of the cornstarch extruded at feed moisture contents of 18.3 and 26.1% (db), barrel temperatures of 393.2 and 413.2 K, and screw speeds of 200, 300, and 400 rpm.

[Color figure can be viewed in the online issue, which is available at wileyonlinelibrary.com.]

MUMPS solver[81] with a time step size of 0.1 s. Each simulation run was completed in about 18 min on a PC with Intel Core i7 processor with 3.40 GHz and 32 GB RAM.

The conservation of water, gas, vapor, and solid phases in Eqs. 26–29 were solved for the dependent variables ε^{w}, p^{g}, ρ^{v}, and ϕ, respectively; the conservation of energy in Eq. 30 was solved for the dependent variable T; and the poroviscoelasticity Eq. 15 was solved for the dependent variable $\mathbf{u}$. Subsequently, the model was validated by comparing the model results with the experimental data, which were surface temperature, moisture content, and expansion ratio of the extrudates. The coefficient of variation (CV) and the average absolute deviation (AAD) were used to measure the differences between the predicted and the experimental data. The AAD was calculated as

$$AAD = \frac{1}{n}\sum_{i=1}^{n}\left|\left(\frac{X_{exp}-X_{pred}}{X_{exp}}\right)_i\right| \tag{40}$$

where n is the number of the data points, X_{exp} is an experimental value, and X_{pred} is the predicted value.

Results and Discussion

The experimental results for the surface temperature, moisture content, and expansion ratio were compared with the modeling results. The purpose of this validation was to test the numerical code for solving the unsaturated transport—poroviscoelasticity model of Takhar[42] for prediction of moisture content, temperature, and expansion ratio in cornstarch extrudate.

Surface temperature distribution

Figure 3 shows the comparisons between the experimental and predicted surface temperature of the extrudates. The experimental surface temperature of extrudates after leaving the die quickly increased and then decreased gradually as the distance from die exit increased while the simulated surface temperature showed only the decreasing trend after exiting the die. Rising temperature may have been caused by a lag in temperature increase that was occurring when the extrudate was passing through the die. In the model, the initial conditions were taken at the moment starch exited the die. The experimental results agree well with the predicted results as confirmed by the AAD that was less than 2.6%. In addition, the model's ability to predict the surface temperature of the extrudates was confirmed by CV that varied between 0.8 and 2.9% (Figure 3). Therefore, there was a good agreement between the predicted and the experimental data as indicated by low AAD and CV. Comparison of the experimental values of average surface temperature of the extrudates at different screw

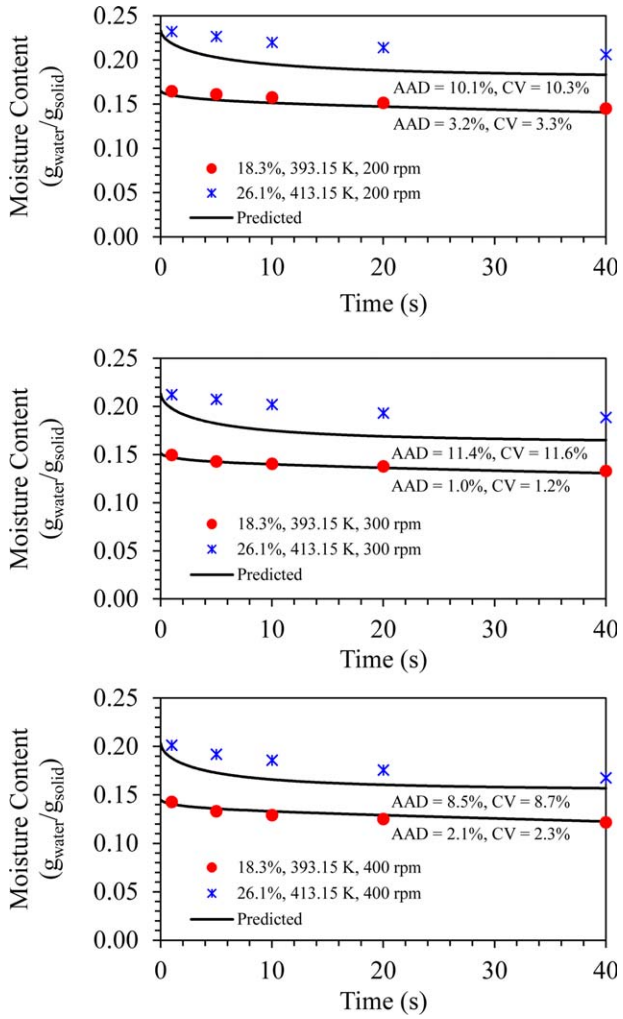

Figure 4. Comparison of experimental and predicted moisture content of the cornstarch extruded at feed moisture contents of 18.3 and 26.1% (db), barrel temperatures of 393.2 and 413.2 K, and screw speeds of 200, 300, and 400 rpm.

[Color figure can be viewed in the online issue, which is available at wileyonlinelibrary.com.]

speeds (Figure 3), showed that the screw speeds had no significant effect on the average experimental surface temperature of the extrudates at feed moisture content of 18.3% (db) and barrel temperature of 393.2 K and at feed moisture content of 26.1% (db) and barrel temperature of 413.2 K after exiting the die at 3.3 and 1.1 s, respectively ($P > 0.05$). The predicted surface temperatures of the extrudates at different screw speeds were significantly different.

Moisture Distribution. The predicted average moisture content values are plotted together with the experimental results in Figure 4. The moisture content trends predicted by the model were found to be consistent with the experimental values with both showing a decreasing trend. The CV for the average moisture content of the extrudates at feed moisture content of 18.3% (db) and barrel temperature of 393.2 K and at feed moisture content of 26.1% (db) and barrel temperature of 413.2 K were 1.2–3.3 and 8.7–11.6%, respectively. Similarly, the AAD for the average moisture content of the extrudates at feed moisture content of 18.3% (db) and barrel temperature of 393.2 K and at feed moisture content of 26.1% (db) and barrel temperature of 413.2 K were 1.0–3.2 and 8.5–11.4%, respectively. The prediction of moisture content of the cornstarch extruded at feed moisture content of 26.1% (db) and barrel temperature of 413.2 K was less accurate. This could have resulted since the equation for coefficient of diffusivity was based upon the experimental data in the temperature range of 333.2–393.2 K.[55] The diffusivity equation used in the model was extrapolated to the higher temperature range (>393.2 K).

Simulated temperature and moisture profiles

The predicted T_{gl} of extrudate increased from 325.9 to 348.5 K because of reduction in water content of the extrudate after exit from the die. The average temperature of extrudates decreased from 419.8 to 322.6 K in 40 s (Figure 5a) and the average volume fraction of water decreased from 0.236 to 0.170 in 40 s (Figure 5b). After exit from the die, extrudate is considered in the rubbery state (solid line). It turned into the glassy state (dash line) when the volume fraction of water became less than 0.178, which occurred beyond 15.8 s after exit from the die. At this time, the average temperature of extrudate was lower than T_{gl} (<344.5 K).

The predicted change in the temperature profile across the radial cross-section of the extrudate at various times is shown in Figure 6a. After exit from the die, the temperature near the

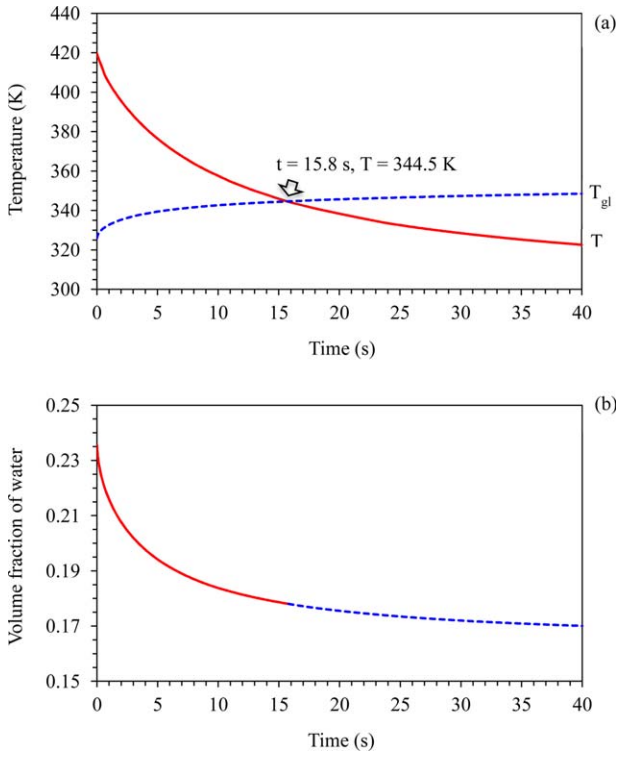

Figure 5. Simulated data of cornstarch extruded at feed moisture content of 26.1% (db), barrel temperature of 413.2 K, and screw speed of 300 rpm: (a) changes in average and glass transition temperatures with time and (b) average volume fraction of water. The solid and dash lines represent the rubbery and glassy states of the extrudate, respectively.

[Color figure can be viewed in the online issue, which is available at wileyonlinelibrary.com.]

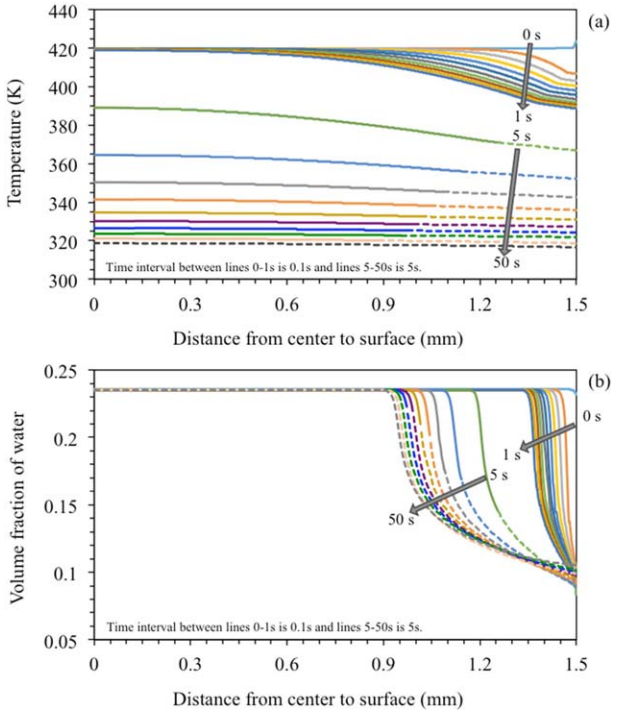

Figure 6. Simulated data of cornstarch extruded at feed moisture content of 26.1% (db), barrel temperature of 413.2 K, and screw speed of 300 rpm; (a) temperature profiles and (b) volume fraction of water profiles across the radial cross-section of a single extrudate. The solid and dash lines represent the rubbery and glassy states of the extrudate, respectively.

[Color figure can be viewed in the online issue, which is available at wileyonlinelibrary.com.]

surface layers reduced rapidly but the temperature near the center reduced slowly. For example, for the extrudate at 5 s after exiting the die, the locations near the surface layers (1.26 mm from center to the surface) were in the glassy state (dash line) but the inside layers (distance from center to 1.26 mm) remained in the rubbery state. The solid lines from $t = 0$–1 s show that the extrudate at all spatial locations were completely in the rubbery state while the whole extrudate turned into the glassy state at 50 s or more after exit from the die. Correspondingly, Figure 6b shows that when the extrudate exited the die, (1) it was in the rubbery state ($t = 0$–1 s); (2) it started changing to the glassy state from the surface to the center ($5 \leq t \leq 45$ s); and (3) it was completely in the glassy state at $t \geq 50$ s. Furthermore, the volume fraction of water at the surface dropped very rapidly due to high evaporation rate.[82] The volume fraction of water near the center dropped slowly due to formation of dry layer near the surface (crust), which became thicker with time. The crust had lower diffusion coefficient of water and water permeability values as compared to the core, which caused the decrease in the rate of mass and heat transfer. Therefore, the volume fraction of water and/or average temperature of the extrudates cannot be used as the indicators to define their states. Determination of the states requires temperature and/or volume fraction of water at the different spatial locations inside the extrudate, which can be estimated using numerical results from this study.

Expansion ratio

After the high-pressure melt passes through the extruder die, the gelatinized starch embeds in the extruded matrix, the liquid water turns to steam and then evaporates quickly, which helps to form a porous structure.[16,28] The comparisons between the experimental and simulated expansion ratios of the extrudates are shown in Figure 7. The expansion ratios of extrudates increased quickly within 0.5 s after exiting the die because of the rapid change in pressure and then gradually decreased until the constant expansion ratios were reached. These trends can be observed in both simulations and experiments, which show the agreement. The AAD for the expansion ratios of the extrudates at feed moisture content of 18.3% (db) and barrel temperature of 393.2 K and at feed moisture content of 26.1% (db) and barrel temperature of 413.2 K were 15.0–22.4 and 29.1–33.4%, respectively. Additionally, the model's ability to calculate the expansion ratios of the extrudates was confirmed by CV that varied between 15.6 and 35.0%. Fan et al.[28] discussed that the initial temperature, moisture content, and melt viscosity were the dominant factors affecting expansion in starchy extrudates. The mechanical properties of the extrudates, such as coefficient of elasticity and Poisson's ratio, were related to melt viscosity. Further improvement in predictions is expected if these properties are known with greater accuracy.

Figure 8 presents a comparison between experimental and predicted expansion ratios when the extrudates were assumed to be poroelastic and poroviscoelastic materials. It clearly shows that the poroviscoelastic model provides better prediction of expansion trend than the poroelastic model. This is because the extrudate exhibits both viscous and elastic characteristics[63,71] when undergoing expansion. The poroelastic model exhibits a hump in expansion ratio curve at 1.1 cm from die exit. This hump gets relaxed in the poroviscoelastic model, in agreement with the experimental trend.

For the linear viscoelastic component, the average mechanical properties of the extrudates such as the Poisson's ratio (v) and the instantaneous shear modulus (G_0), which is the value of $G(t)$ at $t = 0$, were obtained from independent studies.[70,71] The change in the volume of a sample increased as the Poisson's ratio decreased.[83] Evans and Lips[84] demonstrated that the value of G_0 increased approximately linearly with starch concentration, which implies that higher values of G_0 can be detected at lower moisture content. Chanvrier et al.[85] found that the value of G_0 decreased when the temperature of the cornstarch extrudates increased. Increasing the value of G_0 means an increase in the solid-like behavior. The extrudates exhibit a decreased solid-like behavior when the temperature and moisture content are increased.[63] The sensitivity of the parameters in the linear viscoelastic model to affect the expansion ratio is shown in Figure 9. It is clearly demonstrated that the expansion ratio was a function of the G_0 and v, which depended strongly on the moisture content and temperature of the extrudates. Increase in the values of G_0 and v resulted in decrease in the expansion ratios. Therefore, the mechanical properties play a dominant role in the expansion of the extrudates, which is in agreement with work by Kokini et al.[23] Figure 9 can provide guidance for predictably controlling the expansion behavior as a function of the mechanical properties of the material. Expansion/contraction can further be explained using the pore pressure in the poroviscoelastic matrix as discussed in the next section.

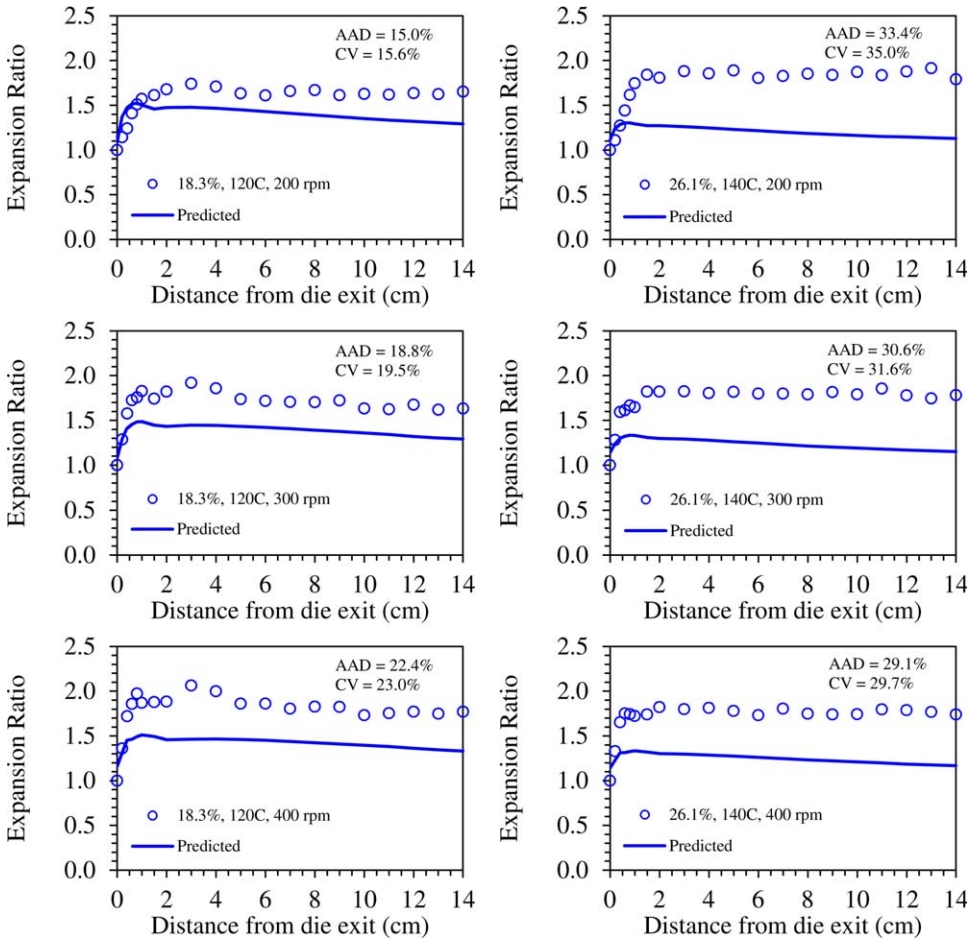

Figure 7. Comparison of experimental and predicted expansion ratio of the cornstarch extruded at feed moisture contents of 18.3 and 26.1% (db), barrel temperatures of 393.2 and 413.2 K, and screw speeds of 200, 300, and 400 rpm.

[Color figure can be viewed in the online issue, which is available at wileyonlinelibrary.com.]

Simulated pressure profiles

Various pressure profiles across the radial cross-section of the extrudate at various times are shown in Figure 10. The predicted gas pressure at the die was 422 kPa (Figure 10a). The extrudate expanded after exit from the die because the gas pressures increased quickly up to 1 s and then started decreasing because of the decrease in temperature of the extrudate due to evaporative cooling and energy loss to the surroundings.

A decrease in moisture content of the extrudate after exit from the die resulted in an increase in the capillary pressure. Figure 10b shows that the capillary pressure near the surface layers increased rapidly while the capillary pressure near the center increased slightly. The high value of capillary pressure near the surface layers can cause the negative water gage pressure (Figure 10c) because the $p^{w} = p^{g} - p^{c}$.

The effect of gas and water pressure on expansion/contraction of matrix can be combined using pore pressure ($p_p = s^{w}p^{w} + s^{g}p^{g}$) (Figure 10d). The extrudate expanded after exiting the die due to pore pressure increase up to 1 s, which was the main driving force for extrudate expansion. The pore pressure of the extrudate near the surface was lower as compared to the center (Figure 10d). The negative water pressure near the surface layers would make the pore pressure negative, which would result in collapse of matrix near the surface. The extrudate expands suddenly after its exit from the die as the pore pressure is much higher than the viscoelastic stress to

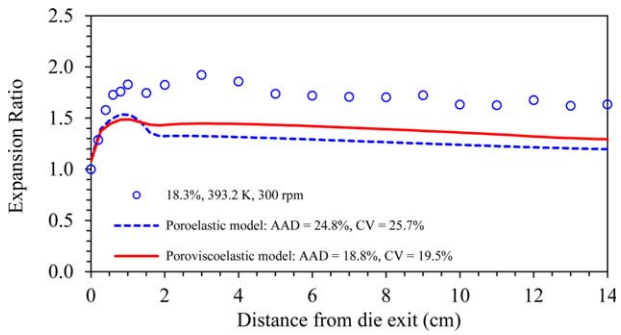

Figure 8. Experimental and predicted expansion ratio obtained on the basis of the poroviscoelastic and poroelastic models of the cornstarch extruded at feed moisture content of 18.3% (db), barrel temperature of 393.2 K, and screw speed of 300 rpm.

[Color figure can be viewed in the online issue, which is available at wileyonlinelibrary.com.]

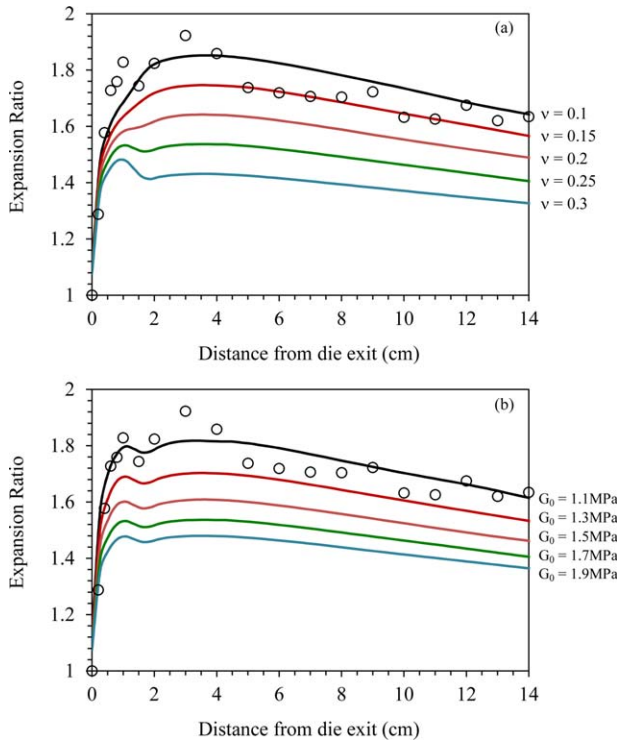

Figure 9. Expansion ratio at various: (a) Poisson's ratio and (b) instantaneous shear modulus of the cornstarch extruded at feed moisture content of 18.3% (db), barrel temperature of 393.2 K and screw speed of 300 rpm.

[Color figure can be viewed in the online issue, which is available at wileyonlinelibrary.com.]

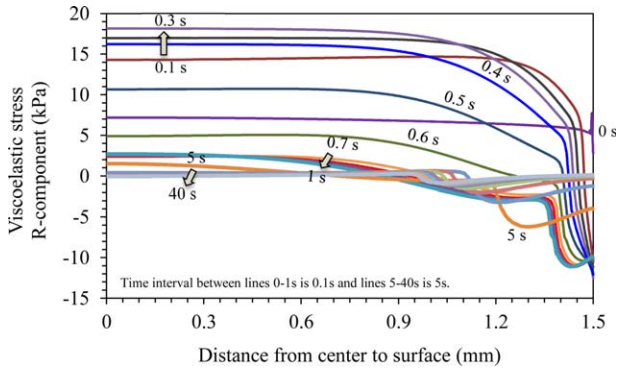

Figure 11. Spatial distribution of *R*-component of viscoelastic stress across the radial cross-section of the cornstarch extruded at feed moisture content of 26.1% (db), barrel temperature of 413.2 K, and screw speed of 300 rpm.

[Color figure can be viewed in the online issue, which is available at wileyonlinelibrary.com.]

make the positive total stress (see Eqs. 16, 17; Figure 11). Next, the matrix expansion slows down and finally it comes to a stop when the total stress becomes equal to zero ($\boldsymbol{\sigma}_p = \boldsymbol{\sigma}_{viscoelas}$). The matrix collapses when the total stress becomes negative ($\boldsymbol{\sigma}_p < \boldsymbol{\sigma}_{viscoelas}$). Thus, control of mechanical and textural attributes of extruded products can be predictably controlled to obtain end-products with different characteristics by studying the effect of extrusion parameters on pore pressure and viscoelastic stress.

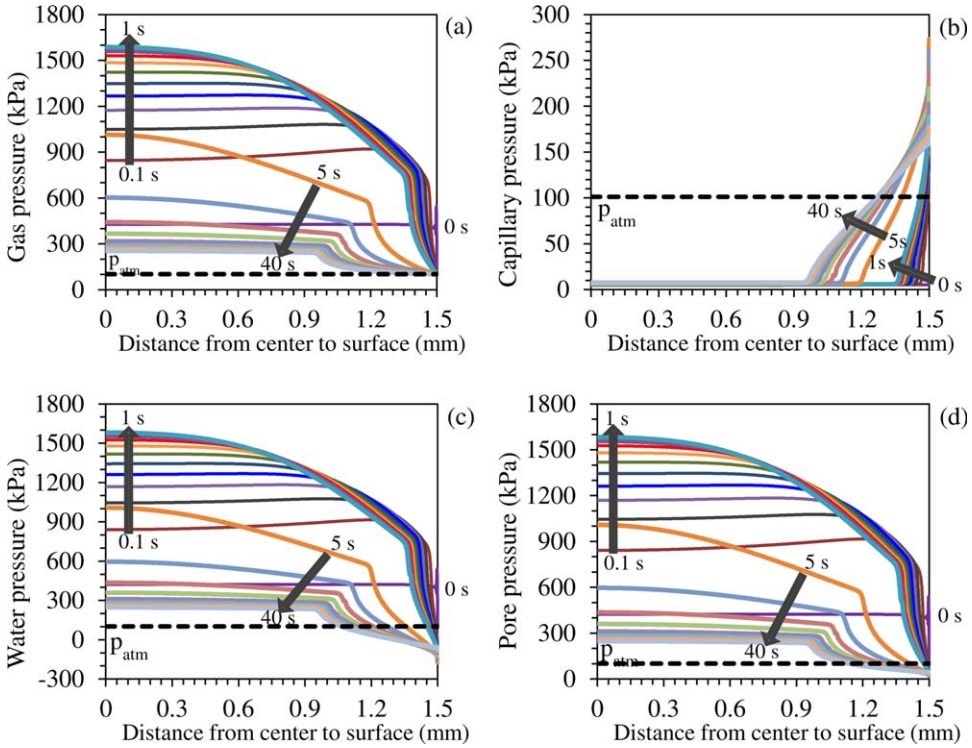

Figure 10. Spatial distribution of (a) gas, (b) capillary, (c) water, and (d) pore pressures across the radial cross-section of the cornstarch extruded at feed moisture content of 26.1% (db), barrel temperature of 413.2 K and screw speed of 300 rpm.

[Color figure can be viewed in the online issue, which is available at wileyonlinelibrary.com.]

Conclusions

The HMT-based model was developed to investigate the expansion phenomenon of the cornstarch extrudates. The extrudate was treated as a porous medium, which was composed of three phases: solid, liquid water, and gas (mixture of water vapor and dry air). The model consisted of coupled two-scale multiphase equations of mass, momentum, and energy transport along with the poroviscoelasticity equations. At microscale, the solid phase was assumed to be a viscoelastic solid and the fluid phases were considered as the viscous fluids. At macroscale, the viscoelastic solid interacted with the viscous fluids in the pores to create a poroviscoelastic system. Mass transfer was driven by pressure and concentration gradients, which included the diffusion between air and vapor phases, bulk and capillary flows, and phase change in terms of evaporation/condensation. Heat was transferred by conduction and convection with phase change playing an important role. The transport equations, which involved both liquid water and gas phases moving through the extrudate matrix, were transformed from the Eulerian coordinates to the Lagrangian coordinates. Correspondingly, the volume change of the extrudate, which occurred due to expansion, was assumed to be geometrically similar to its original cylindrical shape. The volume fraction of water, gas pressure, vapor density, porosity, temperature, and displacement field were considered as the dependent variables in the simulations. The values of surface temperature, moisture content, and expansion ratio of the extrudates at different extrusion conditions were determined for model validation. Simulation results compared well with the experimental results (AAD = 0.7–33.4% and CV = 0.8–35.0%).

When the extrudate exited the die, the glass transition temperature increased as the moisture content of the extrudates deceased. In general, the average values of temperature and/or volume fraction of water can be used to indicate the state (glassy or rubbery) of the materials. However, the simulation results showed that these average values were not a good measure of the state because of nonuniform temperature and/or volume fraction of water at different spatial locations across the cross-section of the extrudate.

Furthermore, the simulated temperature, moisture content, and pressure distribution within the extrudate were investigated. The temperature and moisture content dropped very rapidly from the surface to the interior. It can be seen that the glassy crust was developed from the surface to interior hence the rates of mass and heat transfer decreased due to lower diffusion coefficient of water and water permeability values of the crust. Additionally, the extrudates expanded after exiting the die due to pore pressure development inside the extrudate matrix. Expansion/contraction occurred due to difference between the stress due to pore pressure (σ_p) and viscoelastic stress ($\sigma_{viscoelas}$). At the beginning, the starch expanded rapidly in a few second after exiting the die, as the total stress was positive due to an increase in pore pressure. After that, the pore pressure continued to drop so the extrudate growth slowed down and finally stopped expanding when the total stress became zero. Next, the extrudate started collapsing when the total stress became negative due to $\boldsymbol{\sigma}_p < \boldsymbol{\sigma}_{viscoelas}$. The model obtained in this study can be used for design or modification of the specific texture characteristics of expanded products, and optimizing and/or controlling the process conditions.

Acknowledgment

The authors acknowledge the National Science Foundation for providing financial support under award no. 0756762.

Notation

a_w = water activity, decimal
c_{gl} = constant in Eq. 39, dimensionless
C_p^α = specific heat of the α-phase, J kg^{-1} K^{-1}
db = dry basis
D = diameter of the material, m
D^α = coefficient of diffusivity of the α-phase, m^2 s^{-1}
E = Young's modulus or coefficient of elasticity, Pa
${}^\beta\hat{e}^\alpha$ = net rate of mass gained by the β-phase from α-phase, kg m^{-3} s^{-1}
$\mathbf{F}_b$ = body force, N m^{-3}
g = acceleration due to gravity, m s^{-2}
G_0 = instantaneous shear modulus, Pa
G_m = relaxation modulus of the mth component in relaxation function, Pa
$G(t)$ = relaxation function, Pa
G_∞ = elastic part of relaxation function, Pa
h_m = mass-transfer coefficient, m s^{-1}
h_T = heat-transfer coefficient, W m^{-2} K^{-1}
$\mathbf{I}$ = identity matrix
j = Jacobian, dimensionless
k^α = thermal conductivity of the α-phase, W m^{-1} K^{-1}
K^g = permeability of the gas phase, m^2
K^w = permeability of the water phase, m^2
L = length of the material, m
Le = Lewis number, dimensionless
M^α = molecular weight of the α-phase, kg mol^{-1}
Nu = Nusselt number, dimensionless
N^w = mixture viscosity of the material, Pa s
p_{atm} = atmospheric pressure, Pa
p^c = capillary pressure, Pa
p_p = pore pressure, Pa
Pr = Prandtl number, dimensionless
p_{sat} = saturated vapor pressure, Pa
p_{eq}^v = pressure of vapor phase at equilibrium, Pa
p^α = partial pressure of the α-phase, Pa
Q_T = heat flux, W m^{-2}
Q_v = vapor flux, kg m^{-2} s^{-1}
Q_w = water flux, kg m^{-2} s^{-1}
Ra = Rayleigh number, dimensionless
REV = representative elementary volume, m^3
R_u = universal gas constant, J mol^{-1} K^{-1}
R^2 = coefficient of determination, dimensionless
Re = Reynolds number, dimensionless
R_H = relative humidity, decimal
R^α = specific gas constant for the α-phase, J kg^{-1} K^{-1}
Sc = Schmidt number, dimensionless
s^α = degree of the saturation by the α-phase, dimensionless
t = time, s
T = temperature, K
T_{atm} = atmospheric temperature, K
T_f = film temperature, K
T_{gl} = glass transition temperature, K
T_{gl}^α = glass transition temperature of the α-phase, K
$\mathbf{u}$ = displacement field, m
X_{bw} = mass fraction of bound water (dry basis), $kg_{water}kg_{solid}^{-1}$
X_w = mass fraction of water (dry basis), $kg_{water}kg_{solid}^{-1}$

Greek symbols

ε^α = volume fraction of the α-phase, dimensionless
β = thermal expansion coefficient, K^{-1}
ρ^α = density of the α-phase, kg m^{-3}
μ^α = viscosity of the α-phase, Pa s
ν = Poisson's ratio, dimensionless
$\mathbf{v}^\alpha$ = velocity of the α-phase, m s^{-1}
ϕ = porosity of the material, dimensionless
λ = latent heat of vaporization, J kg^{-1}
ζ = displacement coefficient, dimensionless
ξ = evaporation rate constant, kg m^{-3} s^{-1} Pa^{-1}
$\boldsymbol{\sigma}$ = stress tensor, Pa
τ_m = relaxation time of the mth component in relaxation function, s
$\boldsymbol{\varepsilon}$ = strain tensor, dimensionless

Special symbols

dv^s = Eulerian volume of the solid phase, m^3
dv = Eulerian volume of the material, m^3
dV = Lagrangian volume of the material, m^3
$\hat{e}_r, \hat{e}_\theta, \hat{e}_Z$ = unit vectors in Eulerian coordinates
$\hat{e}_R, \hat{e}_\Theta, \hat{e}_Z$ = unit vectors in Lagrangian coordinates
LHS = left-hand side
RHS = right-hand side
$\mathbf{v}_{\alpha\ s}$ = velocity of the α-phase relative to the solid phase, m s^{-1}
∇_E = spatial gradient in Eulerian coordinate, m^{-1}
∇_L = spatial gradient in Lagrangian coordinate, m^{-1}
dot $(\cdot)$ = material time derivative following the solid phase motion (D^s/Dt), s^{-1}

Subscripts

0 = reference state
amb = ambient
bw = bound water or non-freezing water
E = Eulerian coordinate
eq = equilibrium
gl = glass transition
i = initial state
L = Lagrangian coordinate
M = Maxwell unit
P = denotes pore-pressure or stress due to pore pressure
viscoelas = viscoelastic

Superscripts

g = gas phase
s = solid phase
v = vapor phase
w = water phase
α = general representation of a phase
β = general representation of a phase

LITERATURE CITED

1. Patil RT, Berrios JJ, Tang J, Swanson BB. Evaluation of methods for expansion properties of legume extrudates. *Appl Eng Agric*. 2007;23(6):777–783.
2. Park KB. *Elucidation of Extrusion Puffing Process*, Urbana-Champaign, IL, U.S.A.: University of Illinois, 1976.
3. Colonna P, Melcion JP, Vergnes B, Mercier C. Flow, Mixing and residence time distribution of maize starch within a twin-screw extruder with a longitudinally-split barrel. *J Cereal Sci*. 1983;1(2): 115–125.
4. Harper JM. *Extrusion of Foods, Vol 2*. Boca Raton, FL: CRC Press, 1981.
5. Kokini JL, Chang CN, Lai CS. The role of rheological properties on extrudate expansion. In: Kokini JL, Ho C, Karwe MV, editors. *Food Extrusion Science and Technology*. New York: Marcel Dekker, 1992:631–652.
6. Ganjyal GM, Hanna MA. Role of blowing agents in expansion of high-amylose starch acetate during extrusion. *Cereal Chem J*. 2006; 83(6):577–583.
7. Anderson RA, Conway HF, Peplinski AJ. Gelatinization of corn grits by roll cooking, extrusion cooking and steaming. *Starch Stärke*. 1970;22(4):130–135.
8. Holay SH, Harper JM. Influence of the extrusion shear environment on plant protein texturization. *J Food Sci*. 1982;47(6):1869–1874.
9. Fletcher SI, Richmond P, Smith AC. An experimental study of twin-screw extrusion-cooking of maize grits. *J Food Eng*. 1985;4(4):291–312.
10. Chinnaswamy R, Hanna MA. Relationship between amylose content and extrusion-expansion properties of corn starch. *Cereal Chem*. 1988;65(2):138–143.
11. Bhattacharya M, Hanna MA. Kinetics of starch gelatinization during extrusion cooking. *J Food Sci*. 1987;52(3):764–766.
12. Mercier C, Feillet P. Modification of carbohydrate components by extrusion cooking of cereal products. *Cereal Chem*. 1975;52(3):283–297.
13. El-Dash AA, Gonzales R, Ciol M. Response surface methodology in the control of thermoplastic extrusion of starch. *J Food Eng*. 1983; 2(2):129–152.
14. Gomez MH, Aguilera JM. Changes in the starch fraction during extrusion-cooking of corn. *J Food Sci*. 1983;48(2):378–381.
15. Davidson VJ, Paton D, Diosady LL, Spratt WA. Residence time distributions for wheat starch in a single screw extruder. *J Food Sci*. 1983;48(4):1157–1161.
16. Valle GD, Vergnes B, Colonna P, Patria A. Relations between rheological properties of molten starches and their expansion behaviour in extrusion. *J Food Eng*. 1997;31(3):277–295.
17. Chinnaswamy R, Hanna MA. Relationship between viscosity and expansion properties of variously extrusion-cooked corn grain components. *Food Hydrocolloids*. 1990;3(6):423–434.
18. Lai LS, Kokini JL. Physicochemical changes and rheological properties of starch during extrusion. (A review). *Biotechnol Progr*. 1991; 7(3):251–266.
19. Hoseney RC, Mason WR, Lai CS, Guetzla J. Factors affecting the viscosity and structure of extrusion-cooked wheat starch. In: Kokini JL, Ho C, Karwe MV, editors. *Food Extrusion Science and Technology*. New York: Marcel Dekker, 1992:277–305.
20. Guy RCE, Horne AW. Extrusion and co-extrusion of cereals. In: Blanshard JMV, Mitchell JR, editors. *Food Structure: Its Creation and Evaluation*. London: Butter-Worth Press, 1988:331–349.
21. Baud B, Colonna P, Della Valle G, Roger P. Macromolecular degradation of extruded starches measured by HPSEC-MALLS. In: Barsby TL, Donald AM, Frazier PJ, editors. *Starch: Advances in Structure and Function*. Cambridge, UK: The Royal Society of Chemistry, 2001:40–44.
22. Chinnaswamy R. Basis of cereal starch expansion. *Carbohydr Polym*. 1993;21(2–3):157–167.
23. Kokini JL, Ho C, Karwe MV. *Food Extrusion Science and Technology*. New York: Marcel Dekker, 1992.
24. Colonna P, Tayeb J, Mercier C. Extrusion cooking of starch and starchy products. In: Mercier C, Linko CP, Harper JM, editors. *Extrusion Cooking*. St. Paul, MN, U.S.A.: American Association of Cereal Chemists Publisher, 1989:247–319
25. Harper JM, Tribelhorn RE. Expansion of native cereal starch extrudates. In: Kokini JL, Ho C, Karwe MV, editors. *Food Extrusion Science and Technology*. New York: Marcel Dekker, 1992:653–666.
26. Mitchell JR, Areas JAG. Structural changes in biopolymers during extrusion. In: Kokini JL, Ho C, Karwe MV, editors. *Food Extrusion Science and Technology*. New York: Marcel Dekker, Inc., 1992:345–360.
27. Lee S. *Foam Extrusion: Principles and Practice*. Boca Raton, FL: CRC Press, 2000.
28. Fan J, Mitchell JR, Blanshard JMV. A computer simulation of the dynamics of bubble growth and shrinkage during extrudate expansion. *J Food Eng*. 1994;23(3):337–356.
29. Shafi MA, Lee JG, Flumerfelt RW. Prediction of cellular structure in free expansion polymer foam processing. *Polym Eng Sci*. 1996; 36(14):1950–1959.
30. Wang L, Ganjyal GM, Jones DD, Weller CL, Hanna MA. Modeling of bubble growth dynamics and nonisothermal expansion in starch-based foams during extrusion. *Adv Polym Technol*. 2005;24(1):29–45.
31. Mao D, Edwards JR, Harvey A. Prediction of foam growth and its nucleation in free and limited expansion. *Chem Eng Sci*. 2006;61(6): 1836–1845.
32. Gray WG, Hassanizadeh SM. Paradoxes and realities in unsaturated flow theory. *Water Resour Res*. 1991;27(8):1847–1854.
33. Cushman JH. *The Physics of Fluids in Hierarchical Porous Media: Angstroms to Miles*. Dordrecht, Boston: Kluwer Academic Publishers, 1997.
34. Hornung U. *Homogenization and Porous Media*. New York: Springer, 1997.
35. Whitaker S. Simultaneous heat, mass, and momentum transfer in porous media: a theory of drying. *Adv Heat Trans*. 1977;13:119–203.
36. Coleman B, Noll W. The thermodynamics of elastic materials with heat conduction and viscosity. *Arch Ration Mech Anal*. 1963;13(1): 167–178.
37. Hassanizadeh M, Gray WG. General conservation equations for multi-phase systems: 1. averaging procedure. *Adv Water Resour*. 1979;2:131–144.
38. Achanta S, Cushman JH, Okos MR. On multicomponent, multiphase thermomechanics with interfaces. *Int J Eng Sci*. 1994;32(11):1717–1738.
39. Bennethum LS, Cushman JH. Multiscale, hybrid mixture theory for swelling systems—I: balance laws. *Int J Eng Sci*. 1996;34(2):125–145.
40. Singh PP, Cushman JH, Maier DE. Three scale thermomechanical theory for swelling biopolymeric systems. *Chem Eng Sci*. 2003; 58(17):4017–4035.

41. Singh PP, Cushman JN, Bennethum LS, Maier DE. Thermomechanics of swelling biopolymeric systems. *Transp Porous Media*. 2003;53(1):1–24.
42. Takhar PS. Unsaturated fluid transport in swelling poroviscoelastic biopolymers. *Chem Eng Sci*. 2014;109:98–110.
43. Yortsos YC, Stubos AK. Phase change in porous media. *Curr Opin Colloid Interface Sci*. 2001;6(3):208–216.
44. Stephan P, Kern J. Evaluation of heat and mass transfer phenomena in nucleate boiling. *Int J Heat Fluid Flow*. 2004;25(2):140–148.
45. Bennethum LS, Cushman JH. Coupled solvent and heat transport of a mixture of swelling porous particles and fluids: single time-scale problem. *Transp Porous Media*. 1999;36(2):211–244.
46. Bird RB, Stewart WE, Lightfoot EN. *Transport Phenomena*, *2nd ed*. New York, NY: Wiley, 2002.
47. Vafai K, Tien HC. A numerical investigation of phase change effects in porous materials. *Int J Heat Mass Transfer*. 1989;32(7):1261-1277.
48. De Vries DA. Simultaneous transfer of heat and moisture in porous media. *Trans Am Geophys Union*. 1958;39(5):909–916.
49. Li C, Borja RI, Regueiro RA. Dynamics of porous media at finite strain. *Comput Methods Appl Mech Eng*. 2004;193(36–38):3837–3870.
50. Netti PA, Travascio F, Jain RK. Coupled macromolecular transport and gel mechanics: poroviscoelastic approach. *AIChE J*. 2003;49(6):1580–1596.
51. Ehlers W, Bluhm J. *Porous Media: Theory, Experiments and Numerical Applications*. Berlin: Springer, 2002.
52. Riande E, Diaz-Calleja R, Prolongo M, Masegosa R, Salom C. *Polymer Viscoelasticity: Stress and Strain in Practice*. New York: Marcel Dekker, 2000.
53. Chung TJ. *Applied Continuum Mechanics*. New York: Cambridge University Press, 1996.
54. Eringen AC. *Mechanics of Continua*. Huntington, New York: Robert E. Krieger Publishing Company, 1980.
55. Vagenas GK, Karathanos VT. Prediction of the effective moisture diffusivity in gelatinized food systems. *J Food Eng*. 1993;18(2):159–179.
56. Bolz RE, Tuve GL. *CRC Handbook of Tables for Applied Engineering Science*, *2nd ed*. Boca Ratón, FL: CRC Press, 1973.
57. Poling BE, Prausnitz JM, O'Connell JP. *The Properties of Gases and Liquids*: McGraw-Hill, New York, 2001.
58. Denny MW. *Air and Water: The Biology and Physics of Life's Media*. New Jersey: Princeton University Press, 1993.
59. Zábranský M, Růžička V, Domalski ES. Heat capacity of liquids: critical review and recommended values. Supplement I. *J Phys Chem Ref Data*. 2002;30(5):1199–1689.
60. Vargnaftik NB. *Tables of Thermophysical Properties of Liquids and Gases: in Normal and Dissociated States*, *2nd ed*. Washington: Hemisphere Publishing, 1975.
61. Fang G, Ward CA. Temperature measured close to the interface of an evaporating liquid. *Phys Rev E*. 1999;59(1):417–428.
62. Stanish MA, Schajer GS, Kayihan F. A mathematical model of drying for hygroscopic porous media. *AIChE J*. 1986;32(8):1301–1311.
63. Ditudompo S, Takhar PS, Ganjyal GM, Hanna MA. The effect of temperature and moisture on the mechanical properties of extruded cornstarch. *J Texture Stud*. 2013;44(3):225–237.
64. Perry RH, Green DW. *Perry's Chemical Engineers' Handbook, 7th ed*. New York: McGraw-Hill, 1997.
65. Ni H, Datta AK, Torrance KE. Moisture transport in intensive microwave heating of biomaterials: a multiphase porous media model. *Int J Heat Mass Transfer*. 1999;42(8):1501–1512.
66. Feng H, Tang J, Plumb OA, Cavalieri RP. Intrinsic and relative permeability for flow of humid air in unsaturated apple tissues. *J Food Eng*. 2004;62(2):185–192.
67. Hwang CH, Heldman DR, Chao RR, Taylor TA. Changes in specific heat of corn starch due to gelatinization. *J Food Sci*. 1999;64(1):141–144.
68. Ricardo DAP, Roberto LM, Carmen EPC. Models of Sorption Isotherms for Food: Uses and Limitations. *Vitae*. 2011;18(3):325–334.
69. Maroulis ZB, Shah KK, Saravacos GD. Thermal conductivity of gelatinized starches. *J Food Sci*. 1991;56(3):773–776.
70. Fan XP, Xu W, Zhou JH, Xiang H. FEM simulation of elastic properties of closed-cell starch extrudate with spherical pores. *Adv Mater Res*. 2011;236:2429–2435.
71. Agbisit R, Alavi S, Cheng E, Herald T, Trater A. Relationships between microstructure and mechanical properties of cellular cornstarch extrudates. *J Texture Stud*. 2007;38(2):199–219.
72. Bonneau P, Puiggali JR. Influence of heartwood-sapwood proportions on the drying kinetics of a board. *Wood Sci Technol*. 1993;28(1):67–85.
73. Kang W, Chung W. Liquid water diffusivity of wood from the capillary pressure-moisture relation. *J Wood Sci*. 2009;55(2):91–99.
74. Takhar PS. Hybrid mixture theory based moisture transport and stress development in corn kernels during drying: coupled fluid transport and stress equations. *J Food Eng*. 2011;105(4):663–670.
75. Yang SM. General correlating equations for free convection heat transfer from a vertical cylinder. Paper presented at the Proceedings of the International Symposium on Heat Transfer, Peking, 1985.
76. Holman JP. *Heat Transfer*. Boston, MA: McGraw Hill Higher Education, 2010.
77. Zhong Z, Sun XS. Thermal characterization and phase behavior of cornstarch studied by differential scanning calorimetry. *J Food Eng*. 2005;69(4):453–459.
78. Shogren RL. Effect of moisture-content on the melting and subsequent physical aging of cornstarch. *Carbohydr Polym*. 1992;19(2):83–90.
79. Gordon M, Taylor JS. Ideal copolymers and the second-order transitions of synthetic rubbers. I. Non-crystalline copolymers. *J Appl Chem*. 1952;2(9):493–500.
80. Ditudompo S. *Multiscale Continuum Thermodynamics Based Modeling of Transport Mechanisms and Starch Expansion During Extrusion: Food Science and Human Nutrition*, University of Illinois at Urbana-Champaign, 2015.
81. Amestoy PR, Duff IS, L'Excellent JY. Multifrontal parallel distributed symmetric and unsymmetric solvers. *Comput Methods Appl Mech Eng*. 2000;184(2–4):501–520.
82. Bouvier JM, Campanella OH. *Extrusion Processing Technology: Food and Non-Food Biomaterials*. Wiley, 2014.
83. Bourne MC. Principles of objective texture measurement. In: Bourne MC, editor. *Food Texture and Viscosity*, *Chapter 4, 2nd ed*. London: Academic Press, 2002:107–188.
84. Evans ID, Lips A. Viscoelasticity of gelatinized starch dispersions. *J Texture Stud*. 1992;23(1):69–86.
85. Chanvrier H, Colonna P, Della Valle G, Lourdin D. Structure and mechanical behaviour of corn flour and starch–zein based materials in the glassy state. *Carbohydr Polym*. 2005;59(1):109–119.

Manuscript received Jan. 16, 2015, and revision received May 29, 2015.